Stan, Cristiana, Cheng Zheng, Edmund Kar-Man Chang, Daniela I.V. Domeisen, Chaim I. Garfinkel, Andrea M. Jenney, Hyemi Kim, Young-Kwon Lim, Hai Lin, Andrew Robertson, Chen Schwartz, Frederic Vitart, Jiabao Wang, and Priyanka Yadav. " Advances in the prediction of MJO-Teleconnections in the S2S forecast systems", Bulletin of the American Meteorological Society (published online ahead of print 2022), accessed Feb 19, 2022, https://doi.org/10.1175/BAMS-D-21-0130.1
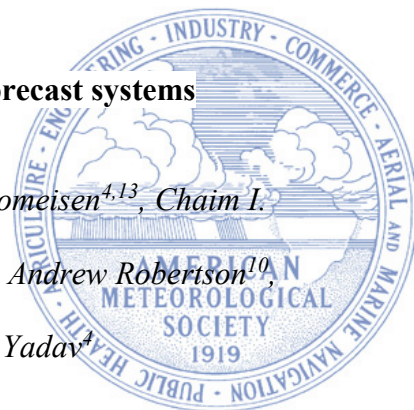
Advances in the prediction of MJO-Teleconnections in the S2S forecast systems

Cristiana Stan[1], Cheng Zheng[2], Edmund Kar-Man Chang[3], Daniela I.V. Domeisen[4,13], Chaim I. Garfinkel[5], Andrea M. Jenney[6], Hyemi Kim[3], Young-Kwon Lim[7,8], Hai Lin[9], Andrew Robertson[10], Chen Schwartz[5], Frederic Vitart[11], Jiabao Wang[12], Priyanka Yadav[4]

[1]Department of Atmospheric, Oceanic and Earth Sciences, George Mason University, USA

[2]Lamont-Doherty Earth Observatory, Columbia University, USA

[3]School of Marine and Atmospheric Sciences, Stony Brook University, USA

[4]ETH Zürich, Institute for Atmospheric and Climate Science, Zürich, Switzerland

[5]The Fredy and Nadine Hermann Institute of Earth Sciences, Hebrew University of Jerusalem, Israel

[6]Department of Earth System Science, University of California, Irvine, USA

[7]Global Modeling and Assimilation Office, NASA Goddard Space Flight Center, USA

[8]Goddard Earth Sciences Technology and Research / University of Maryland Baltimore County, USA

[9]Environment and Climate Change Canada, Canada

[10]International Research Institute for Climate and Society, USA

[11]European Center for Medium-Range Weather Forecast, UK

[12] Center for Western Weather and Water Extremes, Scripps Institute of Oceanography, University of California, San Diego, USA

[13] University of Lausanne, Lausanne, Switzerland

December, 2021

Corresponding author: Cristiana Stan, cstan@gmu.edu

1

Abstract

This study evaluates the ability of state-of-the-art subseasonal to seasonal (S2S) forecasting systems to represent and predict the teleconnections of the Madden Julian Oscillations and their effects on weather in terms of midlatitude weather patterns and North Atlantic tropical cyclones. This evaluation of forecast systems applies novel diagnostics developed to track teleconnections along their preferred pathways in the troposphere and stratosphere, and to measure the global and regional responses induced by teleconnections across both the Northern and Southern Hemispheres. Results of this study will help the modeling community understand to what extent the potential to predict the weather on S2S time scales is achieved by the current generation of forecasting systems, while informing where to focus further development efforts. The findings of this study will also provide impact modelers and decision makers with a better understanding of the potential of S2S predictions related to MJO teleconnections.

Introduction

Since the demonstration of forecast skill in the subseasonal-to-seasonal (S2S) range in the early 2000s (Newman et al., 2003), interest has grown in the societal benefits of these predictions. An international survey conducted by the Global Framework for Climate Services, a United Nation led initiative, to measure the community perspective on climate services, identified S2S forecasts to be more broadly useful to climate decision makers than climate projections (Vangaugh et al. 2016). S2S predictions have been identified as complementary datasets for climate indicators used for characterizing risks from a variety of hazards induced by climate change (White et al., 2017; Vogel et al. 2020). In response to these societal demands, the research and modeling communities have channeled their efforts toward understanding processes in the atmosphere, ocean, land and

2

cryosphere that can be associated with variability on the S2S time scale and building forecast systems with strong skill for this time scale.

For atmospheric variability, the limit of predictability depends on the sources of predictability, which for weather time scales (less than two weeks) come from the memory of the initial atmospheric state of the forecast and for seasonal and longer time ranges come from slowly varying conditions of the land and ocean. For time scales longer than two weeks and shorter than a season, the S2S time scale, the remote impact of patterns of variability through mechanisms known as teleconnections represents a source of predictability, among others.

The tropical and extratropical teleconnections of the Madden-Julian Oscillation (MJO), the dominant mode of intraseasonal variability in the tropics, are considered a major source of predictability on the S2S time scale (Stan et al. 2017). The MJO manifests as a pattern of large-scale convection that begins to organize in the Indian Ocean and propagates eastward along the equator as an oscillation with a period of 30-60 days (Madden and Julian, 1971, 1972). We can imagine the MJO as one of the heat engines of the earth system. When active, this engine powers the atmospheric circulation in the tropics by coupling directly with other sources of energy (e.g., tropical waves) and the atmospheric circulation in the extratropics through poleward propagating Rossby waves.

To understand how MJO teleconnections can be used to improve forecast skill, significant efforts have been dedicated in recent years to developing diagnostics for characterizing the mechanisms and properties of teleconnections along with their impact on weather. For example, in the tropics the MJO can help or hinder the development of tropical cyclones (TCs) in the Atlantic basin in Northern Hemisphere (NH) summer (Maloney and Hartmann, 2000; Camargo et al., 2009; Kosin et al., 2010; Klotzbach, 2010). When the MJO convection is located over Africa and the

western Indian Ocean the TC activity strengthens, while TC activity weakens when MJO convective activity is over the Pacific (Klotzbach and Oliver, 2015). The MJO affects the TC development by reducing the vertical wind shear in the main development region (MDR) of tropical storms. A strong wind shear weakens tropical cyclones by favoring intrusion of dry and cool air into the inner-core of the cyclone. The MJO phase with suppressed convection is accompanied by large areas of subsidence that do not favor development of precipitation thus limiting the growth of developing tropical storms. In the extratropics, the MJO modulates the surface weather by interfering with the large-scale circulation patterns associated with the North Atlantic Oscillation (NAO; Lin et al., 2009; Lin and Brunet, 2009), the Pacific North American Pattern (PNA; Lin, 2015), and the Pacific and Atlantic storm tracks (Guo et al., 2017; Zheng et al. 2018). The interaction between the MJO and the extratropics can take place through Rossby wave propagation in the troposphere or through stratospheric pathways (Garfinkel et al. 2012; Schwartz and Garfinkel 2017; Barnes et al., 2019; Domeisen et al., 2020b). The mediators in the stratospheric pathways are sudden stratospheric warming events (Garfinkel et al., 2012) which affect surface weather through changes in the NAO pattern (Domeisen, 2019). The effect of the MJO on the extratropics tends to prevail during the boreal winter.

Complementary to research efforts for understanding the source of predictability on the S2S time scale, an international modeling database was created to provide the research community access to operational forecast and reforecast (forecast of the past) output. The database is hosted by the S2S Prediction Project (Vitart et al., 2017) and became available in March 2015. Since then all models with the exception of two have been upgraded to newer versions. Some of the most notable updates consist of increasing grid resolution and/or the number of vertical levels, increasing the number of ensemble members, and adding an interactive ocean model to the

4

prediction systems that had been using specified sea surface temperature (SST) to represent the boundary conditions over the oceans. The increase in resolution and the ocean model are expected to improve the representation of mechanisms described as relevant to the MJO teleconnections (Kim et al. 2018).

A basic evaluation of the MJO teleconnections in the first generation of S2S models was performed by Vitart (2017) for the extratropics and Lee et al. (2018) for the TC activity. The evaluation of extratropical teleconnections was conducted using simple statistical diagnostics designed to find coherence between the MJO activity and large-scale circulation patterns in the extratropics without accounting for the mechanisms that explain the teleconnections and confer the source of predictability for the S2S time scale. The evaluation was also limited to the North Atlantic (NA) sector with a brief reference to the North Pacific (NP) region. While the evaluation of MJO-TC relation in Lee et al. (2018) covers all ocean basins, only six S2S models are analyzed.

This paper discusses the capability of state-of-the-art forecasting systems to predict the MJO teleconnections and the ability of the forecast models to then translate the potential predictability of the teleconnections into forecast skill. The evaluation is not designed to compare models against each other, or to rank them.

Overview of models, **reforecast period and verification data**

The operational forecast systems undergo periodic upgrades intended to incorporate research findings that demonstrate a readiness for transition to operations. As a result, the S2S database is periodically updated to reflect the latest model improvements. Depending on the method adopted by each center for generating the reforecast, the reforecasted data sets are also updated. One caveat of this approach is that the upgrades occur at the discretion of operational

centers. To define a common element shared by all S2S models at a particular point in time, this study is based on the model versions used in operations by all centers between June 2019 and July 2020. Table 1 provides a summary of each model's technical descriptions.

The meteorological fields used in this study include the zonal (U) and meridional (V) components of the horizontal wind at multiple levels (850, 500, 100, and 10 hPa), geopotential height at 500 hPa (Z500), air temperature (T) at 500 and 100 hPa, 2-meter air temperature (T2m), and sea level pressure (SLP). All fields with the exception of T2m are instantaneous values. T2m represents a 24-hour average. In addition to these model output variables, the Real-time Multivariate MJO (RMM) index (Wheeler and Hendon, 2004) and its components (RMM1 and RMM2) are downloaded from the S2S database. The RMM index is one of the indices typically used to characterize the amplitude and location of the MJO. In this study, an MJO event is characterized by values of the RMM index ($RMM=[RMM1^2+RMM2^2]^{1/2}$) larger than one standard deviation. The reforecasts are evaluated against the ECMWF Reanalysis ERA-Interim (Dee et al. 2014).

Because in this study the evaluation of MJO teleconnections is deterministic, diagnostics are applied to the ensemble mean of anomalies. We apply diagnostics to ensemble means instead of individual ensemble members to isolate the consistent, and hence least uncertain, component of each models' reforecasts (e.g., Christiansen, 2019). The ensemble mean of reforecast anomalies is computed by averaging the ensemble members of each model. Daily anomalies are computed as deviations from the daily climatology of each reforecast for all the available dates. The robustness of results is evaluated based on a bootstrap analysis (Wilks, 2006) applied to each model. Unless specified, the evaluation is conducted for an extended boreal winter season (November through March) and boreal summer season (May through September).

6

MJO teleconnections to tropical cyclone activity in the North Atlantic basin

Tropical cyclone activity in the NA basin begins in June and lasts through November with a sharp peak from late August through September. For this reason, the analysis of MJO - TC activity is conducted for a season defined between June and November. The MJO influence on the TC activity is evaluated with respect to the daily anomalies in the magnitude of the 200-850 hPa vertical wind shear vector (i.e., $| \mathbf{U}850 - \mathbf{U}200 |$) over the NA basin, similarly to Barnston et al. (2015) and Lim et al. (2016). In this context, large positive anomalies indicate strong westerly or easterly wind shear, while large negative anomalies indicate that vertical wind shear is close to zero. Figures 1 and 2 show the composites of vertical wind shear magnitude anomaly 3 weeks after the MJO's enhanced convection is located: *i*) over the Pacific and Western Hemisphere (phases 7-8) and *ii*) over the Maritime Continent (phases 4-5). In reanalysis, the MJO phases 7-8 are followed by negative vertical shear magnitude anomalies in the MDR (Fig. 1a) and positive anomalies follow phases 4-5 (Fig. 2a). The pattern correlation between the models and observed wind shear magnitude varies between 0.06-0.47 for the reforecasts initialized during the MJO phases 7-8 and 0.17-0.69 for the reforecasts initialized during phases 4-5, with more models (8) showing a correlation above 0.45 for the reforecasts initialized when the MJO convection is located over the Maritime Continent (MC) than the reforecasts initialized when the MJO convection is located over the Pacific and Western Hemisphere (3 models). The weak correlation displayed by the reforecasts initialized during the MJO phases 7-8 can be partly explained by the northward displacement of regions with negative wind shear magnitude relative to the MDR. The same analysis for lead time 2 weeks reveals higher pattern correlations than for lead time 3 weeks. Correlation patterns for week 2 range between 0.30-0.70 for forecasts initialized during the MJO

7

phases 7-8 and between 0.26-0.70 for forecasts initialized during MJO phases 4-5 (Supplementary Figures ES1 and ES2).

The same diagnostic is applied to another key variable for determining the TC activity, the Atlantic SLP anomalies (see Supplementary Figures ES3 and ES4), which in observations are modulated by the MJO phases. Forecasts at 3 weeks lead show that the negative (positive) SLP anomalies prevail over the subtropical to mid-latitude North Atlantic for the reforecasts initialized during the MJO phases 7-8 (4-5), indicating favorable (unfavorable) conditions for TC activity. Forecasts are generally in good agreement with observations, with pattern correlations varying between 0.50-0.80.

MJO teleconnections to the Northern Hemisphere geopotential height distribution

The response of Z500 anomalies to MJO influence is evaluated using both the tropospheric and stratospheric pathways. The analysis first identifies the regions most sensitive to the MJO influence during the boreal winter and summer and then focuses on these regions with an emphasis on the NP sector.

The Sensitivity To the Remote Influence of Periodic EventS (STRIPES) index (Jenney et al., 2019) for Z500 anomalies is used to evaluate the global MJO teleconnections to the extratropics. The STRIPES index measures the strength and consistency (between different MJO events) of the extratropical response to the effects of MJO events as MJO events evolve through their life cycles. The STRIPES index is positively defined and has no upper bound. It is calculated by first taking lagged composites of geopotential heights across all MJO phases for a range of lead times, and then calculating the average magnitude of maxima in composited anomalies for each phase (see Jenney et al., 2019). The propagation of the MJO is included in the calculation of the

index by assuming that the maxima in composited anomalies for an MJO phase occurs between 5-8 days prior to the lead time for the previous MJO phase. Because the STRIPES index shown here is calculated using observed RMM phases at initialization, errors in MJO phase prediction are not included. The higher the value of the index, the stronger the sensitivity of the region to the MJO influence. Figure 3 shows the extratropical regions that in reanalysis display strong sensitivity to the MJO activity during boreal winter and boreal summer, respectively. During boreal winter, the strongest sensitivity manifests over regions along the Atlantic and Pacific storm tracks and Europe. During boreal summer, both the NH and Southern Hemisphere (SH) show regions with strong sensitivities to the MJO activity. In the SH the entire midlatitudes are affected, whereas in the NH the region with the most sensitivity is located in the northern Pacific. The multi-model average of the difference between the week 2-3 STRIPES index of reanalysis and reforecasts indicates some disagreements between the overall extratropical variability simulated by the S2S models and reanalysis. These differences can be linked to the models' ability to simulate the pathways through which the MJO forcing reaches the extratropics and the interaction of the forcing with the background state of the extratropics. Because the STRIPES index quantifies the magnitude and consistency of a region's response to the remote influence of the MJO, a positive (negative) difference indicates that S2S models tend to overestimate (underestimate) the magnitude of the extratropical response and/or the consistency of the extratropical response between MJO events. In general, simulated extratropical STRIPES indices are weaker than observed at week 2-3. To determine the range of sensitivities spanned by the S2S models, the STRIPES index of Z500 for each of the high sensitivity regions is computed for each ensemble of reforecasts and then compared to the observed STRIPES index. Figure 4 summarizes the ability of each model to forecast MJO teleconnections over these regions as a fraction of the observed STRIPES index; i.e.,

the ratio of the STRIPES index between reforecasts and reanalysis. The fraction of the observed STRIPES index corresponding to the most sensitive regions (boxed regions in Figure 3) are shown in Fig. 4. Here, we have calculated the STRIPES index using a sliding 2-week window. During the boreal winter weeks 1-2, most models tend to overestimate the amplitude of teleconnections over all three regions of interest. During the boreal summer weeks 1-2, models overestimate the amplitude of teleconnection in the Z500 field over the Southern Ocean, and are split roughly in half about the ability to forecast the amplitude of teleconnection over the NP. For both seasons by week 2-3, most models forecast a weaker than observed teleconnection response in the Z500 field. For reference, we include figures showing lagged composite Z500 anomalies (as a function of lead time and MJO phase) in the supplemental material (Figures ES5 and ES6 in Supplemental).

Another way to measure the accuracy of a forecast system is through the anomaly correlation, and two diagnostic metrics from Wang et al. (2020) are adopted for this purpose: *i*) the pattern correlation coefficient (pattern CC) and *ii*) the relative amplitude. The pattern CC is calculated between the reanalysis and individual models over the Pacific-North America (PNA) region (120°E-60°W, 20°-80°N) where the MJO-associated Z500 anomalies show large variability (e.g., Fig. 3a). The relative amplitude is defined as the model Z500 anomaly standard deviation over the PNA region divided by that in reanalysis. The calculation of the metrics is performed by first selecting the MJO events based on the reanalysis. Then the metrics are calculated using Z500 anomalies following each MJO event in both reanalysis and reforecasts. Figure 5 shows the average of the metric values over all boreal winter MJO events and the MJO-teleconnections pattern CC as well the relative amplitude in individual S2S models as a function of the forecast lead days for phases 2-3 (active convection is located over the Indian Ocean) and phases 6-7 (suppressed convection is located over the Indian Ocean). The general feature of MJO-

10

teleconnection pattern and its amplitude in the reforecasts is similar among the MJO phases. Pattern CC decreases as the lead time increases and drops below 0.5 when the lead time increases to about 1-2 weeks. This suggests that the prediction of MJO teleconnection patterns is skillful up to two weeks regardless of the MJO phase. Within the first week, the predicted MJO teleconnection amplitude is close to reanalysis. As the lead day increases, models start to underestimate the teleconnection amplitude. At leads from about day 21 to day 32 (beyond three weeks), the predicted MJO teleconnection amplitude drops to about 40 to 70% of the reanalysis.

The composites of Z500 anomalies over the PNA region for weeks 2 and 4 after the MJO phases 2-3 in S2S models and reanalysis are shown in Fig. ES7 (Supplemental). Note that the reanalysis is shown for the same period as for BoM, from 1981-2013 without considering the initialization date to match with S2S models. Generally, S2S models tend to capture the Z500 anomaly patterns well for the first two weeks with a pattern CC over 0.8 for all models. However, some S2S models fail to capture the transition of Z500 anomalies associated with the MJO phases 2-3 to the opposite MJO phases (6-7) after 4 weeks. Signals in the S2S models are mostly weaker in week 4.

In these analyses there is an implicit assumption that the MJO teleconnections can be explained by the poleward propagation of Rossby waves in the upper troposphere (Hoskins and Karoly, 1981). More recent studies suggest that in addition to these tropospheric pathways, stratosphere-troposphere coupling contributes to the MJO signal in the extratropics (Garfinkel et al., 2012; Schwartz and Garfinkel, 2017). The stratospheric circulation is dominantly impacted by waves of tropospheric origin that weaken the stratospheric mean flow, while stratospheric anomalies in turn can have an influence on surface weather. Hence, the stratosphere acts as a bridge for the MJO teleconnection that can be described as consisting of two segments: one segment

11

characterizes the upward wave propagation from the troposphere into the stratosphere, whereas the second segment connects the stratosphere altered by the MJO to the troposphere. Anomalies originating from the MJO forcing can influence the stratosphere through anomalous wave flux into the stratosphere, characterized by the meridional heat flux, which is therefore a useful metric to diagnose the first segment of the stratospheric pathway. The models' ability to forecast this pathway is evaluated in Fig. 6, and the subsequent vortex response and downward propagation in Fig. 7 using the diagnostics defined in Schwartz and Garfinkel (2020). These diagnostics evaluate the anomalies in geopotential height in the mid-troposphere at 500 hPa near the climatological North Pacific low (190-220ºE), as a deeper low in this region has been shown to strengthen upward propagating tropospheric planetary wavenumber one (Garfinkel et al 2010). In addition, these metrics include the planetary (zonal wavenumber one and two) meridional heat flux at 500 and 100 hPa, which is a proxy for the waves in the mid-troposphere (500 hPa) and those that have already entered the stratosphere (100 hPa) and are therefore likely to influence the stratospheric circulation, with enhanced heat flux generally leading to a weaker stratospheric polar vortex. For each diagnostic, we show both the response in the forecast system and the corresponding response in ERA-I after subsampling to select the identical dates included for each model's reforecast and we analyze the difference between reforecasts initialized during active MJO phases 1-2 (enhanced convection over the Indian Ocean) and MJO phases 5-6 (enhanced convection over the Western Pacific).

Over the Northeast Pacific sector models forecast the initial low, but with a slightly lower amplitude in week-2, and do not capture the reversal in weeks 4-5 as the MJO switches phases (Fig. 6a, b). This result is consistent with the findings reveled by the pattern CC for the PNA region. Over the NH polar region, some models capture the observed ridge, but the response is too

12

weak as compared to reanalysis, whereas other models fail to capture this feature especially in the lower stratosphere (Fig. 7c, d). Models do not forecast the signal in week 5 and 6 when the response should reverse. Figures 7a, b and 8 show the response of the stratospheric polar vortex following MJO events. Several models capture the weakening of the vortex around week 4 with an amplitude similar to reanalysis (Fig. 7a, b), but for many models the response is too weak. For many models the distributions of U10 during the two MJO phases are not distinguishable or even opposite to the signal in reanalysis. The poor representation of the stratospheric response in the models can be explained by the models' inability to capture the meridional transport of heat in the middle troposphere (500hPa, Fig. 6c,d) and lower stratosphere (100hPa, Fig 6e,f). At both levels, the poleward heat transport is underestimated by the models in the first few weeks and the reversal of the transport after week 4 is completely missed by the models. Another part of the problem likely arises from differences in the climatological distribution of the polar vortex winds (Fig. 8).

The fidelity of the stratospheric polar vortex predicted by a model shows some dependency on the number of vertical levels and location of the model top (Charlton-Perez et al., 2013; Cai et al. 2017). As shown in Table 1, the number of vertical levels in the S2S models vary from 17 (BoM) to 91 (ECMWF). Prediction systems with fewer levels also tend to have low model tops, e.g., Domeisen et al. (2020a) classified S2S models with less than 60 levels as low-top models. In this study the models defined as low top include BoM, CMA, and CNR-ISAC. These low-top models especially struggle to capture the stratospheric pathway, however even high-top models underestimate its strength.

MJO teleconnections to the Northern Hemisphere storm tracks

13

The NH midlatitude storm track is evaluated using the 24-h difference filtered eddy kinetic energy at 850 hPa following Yau and Chang (2020), and defined as:

$$eke850(t) = \frac{1}{2}\{\overline{[850(t + 24h) - U850(t)]^2} + \overline{[V850(t + 24h) - V850(t)]^2}\} \quad (1)$$

where the overbar denotes a two-week averaging, and U850 and V850 are the zonal and meridional wind at 850 hPa. In (1), U850 and V850 are first filtered using a 24-h difference filter (Wallace et al., 1988), which highlights synoptic scale variability with periods between 1.2 and 6 days. These filtered velocity anomalies are then combined to form *eke*850, the eddy kinetic energy of synoptic time scale variability. As shown by many previous studies, the peaks from this 24- h difference filter lie over geographical locations where extratropical cyclones preferentially cross. Here, the *eke*850 metric represents the eddy kinetic energy associated with extratropical storm tracks. One of the relevant features of the *eke*850 metric is its high correlation with boreal winter precipitation and high wind events (Yau and Chang, 2020). Model composites of *eke*850 for weeks 3-4 are made by selecting reforecast cases when there is an active MJO event at the time of reforecast initialization. An example is shown in Fig. 9a-d for the ECMWF model, which has a good representation of the MJO teleconnections to geopotential height and storm tracks (Figs. 5 and 10). The corresponding reanalysis composites using the same MJO cases are shown in Fig. 9e-h. The average of the 11 composites for all models are shown in Fig. 9i-l, and the average of the 11 reanalysis composites are shown in Fig. 9m-p. Pattern correlation between model composites (e.g., Fig. 9a-d) and the average of the 11 reanalysis composites (Fig. 9m-p) are calculated to evaluate the models' ability to capture the MJO influence on extratropical storm tracks. Overall, models are able to capture some of the MJO impact on storm tracks during weeks 3-4 when the forecasts are initialized in MJO phases 8-1, 2-3 and 4-5 (Fig. 9i-k, m-o), when the pattern correlation is above 0.5. The enhancement of storm track activity (positive anomalies) caused by the MJO is better

14

captured than the weakening of the activity (negative anomalies) in response to the MJO influence. The signal after MJO convection is located over the western Pacific (phases 6-7; Fig. 9l, p) in the models is too weak compared with reanalysis and the pattern correlation is quite low. Note that the response of storm tracks after 3-4 weeks following an MJO event is very different from the response immediately after initialization (see Supplemental Figs. ES8 and ES9).

Given that the storm tracks and large-scale circulation are symbiotic in nature (e.g., Cai and Mak, 1990), the MJO impact on storm track activity is not independent of the MJO impact on the large-scale circulation in the extratropics, which was discussed in the previous diagnostics. Therefore, the models' deficiencies noted in Figs. 3, 4 and 5 can also explain some of the errors seen in the prediction of $eke850$. For consistency of analysis, the models' ability in capturing the MJO impact on the extratropical large-scale circulation is also evaluated by calculating the pattern correlation of the composite maps similar to Fig. 9 but using Z500 anomalies instead of $eke850$. Scatter diagrams are then constructed using the pattern correlations for Z500 anomalies and $eke850$ for the NH (20°-80°N; Fig. 10a-d), the NP and North America (20°-80°N, 120E°-90°W; Fig. 10e-h), as well as the NA (20°-80°N, 90W°-30°E; Fig. 10i-l). Generally, the models that better simulate the MJO impact on the large-scale circulation (Z500) also better capture the MJO impact on extratropical cyclone activity, as the correlation in all panels in Fig. 10, except for Fig. 10f and 10h, is statistically significant at 95%. Also, models generally capture the MJO impact on large-scale circulation better than the MJO influence on storm tracks, as the dots in each panel of Fig. 10 fall below the 1:1 line.

MJO teleconnections to the Northern Hemisphere 2-meter temperature distribution

15

The surface response associated with the teleconnection patterns in the geopotential height and storm tracks is evaluated by analyzing the surface air temperature. The evaluation of S2S models' ability to forecast the MJO influence on the extratropical surface air temperature is conducted using the MJO phase composites of the T2m anomalies averaged for week 3 and week 4 following an MJO event in the initial condition. The week-3 composites corresponding to MJO enhanced convective activity located west of the MC (phase 3) are shown in Fig. 11 and the composites corresponding to suppressed convective activity over the same region (phase 7) are shown in Fig. 12. In this diagnostic, the composites represent models' ability in predicting the teleconnections associated with the MJO.

In reanalysis, the MJO phase 3 is followed by two large areas of warm (positive) temperature anomalies (over North America and western Europe) and a large sector of cold (negative) temperature anomalies (from the Canadian Arctic to Siberia). This distribution of temperature anomalies reverses the sign following the MJO phase 7. Most models forecast the sign and approximate location of centers of temperature anomalies following the MJO phase 3, however, with the exception of one model, the magnitude of temperature anomalies tend to be smaller than in reanalysis (Fig. 11). Following the MJO phase 7 (Fig. 12), models struggle to simulate teleconnections to a similar degree as for those associated with the MJO phase 3. The difference in capturing the observed teleconnection between the two MJO phases suggests that the atmospheric response to the MJO is likely nonlinear and that there may be different dynamical processes involved for the T2m teleconnection to the two MJO phases. Besides the physical non-linearity, these differences can also be related to the models' ability to simulate the observed characteristics of the MJO. The MJO forecast skill of S2S models is limited by the biases in the mean moisture distribution and cloud-longwave feedback processes in the tropics (Lim et al.,

16

2018). These biases slow down the eastward propagation of the MJO (Lim et al., 2018). When a forecast is initialized during MJO phase 7, the location of convection predicted by the model in the first two weeks will have errors, which will affect the extratropical teleconnections in weeks 3 and 4. Results for week 4 are shown in Supplemental Figs. ES10 and ES11.

Conclusions and Recommendations

Advances in model development coupled with new understanding about physical mechanisms controlling the MJO influence on the extratropics show that state-of-the-art S2S forecast systems have the ability to capture not only the MJO teleconnections as shown by Vitart (2017) but also the mechanisms associated with teleconnections. Furthermore, the newer versions of S2S models use the potential predictability of teleconnections as an opportunity to enhance the forecast skill of weather in the extratropical NH. In addition to the MJO teleconnections to the extratropics, models in the S2S database adequately capture the MJO influence on the vertical wind shear that can potentially influence the Atlantic's TC activity. There are also persistent problems in the models that have yet to be improved. Beyond week 2, in the current generation of models, the amplitude of MJO teleconnections to the NP and the Euro-Atlantic sector continues to be underestimated as in the previous versions of the models evaluated by Vitart (2017). In the newer forecasting systems, the amplitude of teleconnections is overestimated in the first two weeks when considering all MJO phases; when only selective MJO phases are considered, e.g., 2-3 and 6-7, during the second week the magnitude of teleconnections becomes weaker. The modest but global overestimation of the amplitude of MJO teleconnections suggests that model biases may be one of the sources of errors. Differences between models and reanalysis also show a seasonal and regional dependence, with the largest overestimates occurring over the Pacific region in winter

17

and around the dateline over the polar Southern Ocean in boreal summer. Reproducing the magnitude of the extratropical response to MJO teleconnections remains a challenge for the S2S forecast systems.

Models with a small number of vertical levels show a narrow distribution of wintertime westerly winds in the polar stratosphere in comparison to reanalysis. Some of the models with a low top also show low skill with respect to metrics related to the tropospheric pathways of teleconnections. Other studies have emphasized the role of stratospheric representation on the forecast skill of MJO teleconnections (e.g., Feng et al. 2021). Consistent with findings of Schwartz and Garfinkel (2020) model development should be focused on improving processes that govern the troposphere-stratosphere coupling.

Tropical and extratropical cyclone activity are two areas for which models show the biggest challenges in exploiting the potential predictability associated with the modulation of cyclone activity by the MJO. More studies focused on the influence of the MJO on the eddy-mean flow interaction are required to understand which model improvements will enhance the forecast skill of storm track activity on S2S time scales.

References:

Barnes, E. A., S. M. Samarasinghe, I. Ebert-Uphoff, and J. C. Furtado, 2019: Tropospheric and stratospheric causal pathways between the MJO and NAO. *J. Geophys. Res.*: *Atmospheres*, **124**, 9356 – 9371. doi:10.1029/2019JD031024.

Barnston, A. G., N. Vigaud, L. N. Long, M. K. Tippet, J.-K. E. Schemm, 2015: Atlantic tropical cyclone in response to the MJO in NOAA's CFS model. *Mon. Wea. Rev.*, **143**, 4905-4927, doi:10.1175/MWR-D-15-0127.1.

Cai, M., and M. Mak, 1990: Symbiotic relation between planetary and synoptic scale waves. *J. Atmos. Sci.*, **47**, 2953-2968.

Cai, Z., K. Wei, L. Xu, X. Lan, W. Chen, D. Nath, 2017: The influences of model configuration on the simulations of stratospheric Northern-Hemisphere polar vortex in the CMIP 5 models. *Adv. Meteorol.*, **2017**, 7326759. doi:10.1155/2017/7326759.

Camargo, S. J., M. C. Wheeler, A. H. Sobel, 2009: Diagnosis of the MJO modulation of tropical cyclogenesis using an empirical index. *J. Atmos. Sci.*, **66**, 3061-3074. doi:10.1175/2009JAS3101.1.

Christiansen, B., 2019: Analysis of ensemble mean forecasts: The blessing of high dimensionality, *Mon. Wea. Rev.*, **147**, 5, 1799-1712. doi:10.1175/MWR-D-18-0211.1

Charlton- Perez, Andrew J., Mark P. Baldwin, Thomas Birner, Robert X. Black, Amy H. Butler, Natalia Calvo, Nicholas A. Davis et al. 2013: On the lack of stratospheric dynamical variability in low- top versions of the CMIP5 models. *J. Geophys. Res.: Atmospheres,* **118**, 2494-2505.

Dee, D. P., S.M. Uppala, A. J. Simmons, P. Berrisford, P. Poli, S. Kobayashi, U. Andrae, M. A. Balmaseda, G. Balsamo, P. bauer, P. Bechtold, A. C. M. Beljaars, L. van de Berg, J. Bidlot, N. Bormann, C. Delsol, R. Dragani, M. Fuentes, A. J. Geer, L. Haimberger, S. B. Healy, H. Herbach, E. V. Hólm, L. Isaksen, P. Kållberg, M. Köhler, M. Matricardi, A. P. McNally, B. M. Monge-Sanz, J.-J. Morcrette, B.-K. park, C. Peubey, P. de Rosnay, C. Tavolato, J.-N. Thépaut, and F. Vitart, 2011: The ERA-Interim reanalysis: configuration and performance of the data assimilation system. *Q. J. Roy. Meteorol. Soc.*, **137**, 553-597. doi: 10.1002/qj.828.

Domeisen, D. I. V., Butler, A. H., Charlton-Perez, A. J., Ayarzaguena, B., Baldwin, M. P., Dunn Sigouin, E., et al., 2020a. The Role of the Stratosphere in Subseasonal to Seasonal Prediction: 1. Predictability of the Stratosphere. Journal of Geophysical Research-Atmospheres, 125(2), 1–17. http://doi.org/10.1029/2019JD030920

Domeisen, D. I. V., A. H. Butler, A. J. Charlton-Perez, B. Ayarzagüena, M. P. Baldwin, E. Dunn-Sigouin, G. I. Garfinkel, P. Hitchcock, A. Y. Karpechko, H. Kim., J. Knight, A. L. Lang,

20

E. -P. Lim, A. Marshall, G. Roff, C. Schwartz, I. R. Simpson, S. -W. Son, M. Taguchi, 2020b: The role of the stratosphere in subseasonal to seasonal prediction: 2. Predictability arising from stratosphere-troposphere coupling. *J. Geophys*. *Res*.: *Atmospheres*, **125**, e2019JD030923. doi:10.1029/2019JD030923.

Domeisen, D. I. V., 2019: Estimating the frequency of sudden stratospheric warming events from observations of the North Atlantic oscillation. *J. Geophys*. *Res*.: *Atmospheres*, **124**, 3180-3194. doi:10.1029/2018JD030077.

Feng, P. -N., H. Lin, J. Derome, T. M. Merlis, 2021: Forecast skill of the NAO in the subseasonal-to-seasonal prediction models. *J. Climate*, **34**, 4757-4769. doi:10.1175/JCLI-D-20-0430.1.

Garfinkel, C. I., S. B. Feldstein, D. W. Waugh, C. Yoo, and S. Lee, 2012: Observed connection between stratospheric sudden warmings and the Madden-Julian Oscillation. *Geophys*. *Res*. *Lett*., **39**, L18807. doi:10.1029/2012GL053144.

Guo, Y., T. Shinoda, J. Lin, and E. K. M. Chang, 2017: Variations of Northern Hemisphere storm track and extratropical cyclone activity associated with the Madden-Julian Oscillations. *J. Climate*, **30**, 4799-4818, doi:10.1175/JCLI-D-16-0513.1.

Hoskins, B. J. and D. J. Karoly, 1981: The steady linear response of a spherical atmosphere to thermal orographic forcing. *J. Atmos*. *Sci*., **38**, 1179-1196.

Jenney, A. M., E. A. Barnes, and D. A. Randall, 2019: Quantifying regional sensitivities to periodic events: Application to the MJO. *J. Geophys*. *Res*., **124**, 3671-3683. doi:10.1029/2018JD029457.

Kim, H., F. Vitart, and D. E. Waliser, 2018: Prediction of the Madden-Julian Oscillation: A review. *J. Climate*, **31**, 9425-9443, doi: 10.1175/JCLI-D-18-0210.1

Klotzbach, P. J., 2010: On the Madden-Julian Oscillation-Atlantic hurricane relationship. J. Climate, 23, 282-293. doi:10.1175/2009JCLI2978.1.

Klotzbach, P. J., and E. C. J. Oliver, 2015: Modulation of Atlantic Basin Tropical Cyclone Activity by the Madden–Julian Oscillation (MJO) from 1905 to 2011. *J. Climate*., **28,** 204–217.

Kossin, J. P., S. J. Camargo, and M. Sitkowski, 2010: Climate modulation of North Atlantic hurricane tracks. *J. Climate*, **23**, 3057-3076. doi:10.1175/2010JCLI3497.1.

Lee, C. -Y, S. Camargo, F. Vitart, A. H. Sobel, and M. K. Tippet, 2018: Subseasonal tropical cyclone genesis prediction and MJO in the S2S dataset. *Wea. Forecast*., **33**, 967-988. doi:10.1175/WAF-D-17-0165.1

Lim, Y.-K., S. D. Schubert, O. Reale, A. M. Molod, M. J. Suarez, and B. M. Auer, 2016: Large-scale controls on Atlantic tropical cyclone activity on seasonal time scales. *J. Climate*, **29**, 6727-6749. doi:10.1175/JCLI-D-16-0098.1.

Lim, Y., Seok-Woo Son, and D. Kim, 2018: MJO prediction skill of the subseasonal-to-seasonal prediction model. *J. Climate*, **31**, 4075-4094. doi:10.1075/JCLI-D-17-0545.1.

Lin, H., and G. Brunet, 2009: The influence of the Madden-Julian oscillation on Canadian wintertime surface air temperature. *Mon. Wea. Rev*., **137**, 2250–2262.

Lin, H., G. Brunet, and J. Derome, 2009: An observed connection between the North Atlantic Oscillation and the Madden-Julian oscillation. *J. Climate.*, **22**, 364–380. doi:10.1175/2008JCLI2515.1.

Lin, H., 2015: Subseasonal variability of North American wintertime surface air temperature. *Clim*ate *Dyn*., **45**, 1137–1155.

Madden, R. A. and P. R. Julian, 1971: Detection of a 40-50 day oscillation in the zonal wind in the tropical Pacific. *J. Atmos. Sci*., **28**, 702-708.

Madden, R.A., and P. R. Julian, 1972: Description of global-scale circulation cells in the tropics with a 40-50 day period. *J. Atmos. Sci.*, **29**, 1109-1123.

Maloney, E. D., and D. L. Hartmann, 2000: Modulation of hurricane activity in the Gulf of Mexico by the Madden-Julian oscillation. *Science*, **287**, 2002-2004. doi:10.1126/287.5460.2002.

Newman, M., P. D. Sardeshmukh, C. R. Winkler, J. S. Whitaker, 2003: A study of subseasonal predictability. *Mon. Wea. Rev.*, **131**, 1715-1732. doi:10.1175/25581.1.

Klotzbach, P. J., and E. J. Oliver, 2015: Modulation of Atlantic basin tropical cyclone activity by the Madden-Julian oscillation (MJO) from 1905 to 2011. *J. Climate*, **28**, 204-217. doi: 10.1175/JCLI-D-14-00509.1.

Schwartz, C., and C. I. Garfinkel, 2020: Troposphere-stratosphere coupling in subseasonal-to-seasonal models and its importance for a realistic extratropical response to the Madden-Julian oscillation. *J. Geophys. Res.*, **125**, e2019JD032043. doi:10.1029/2019JD032043.

Stan, C., D. M. Straus, J.S. Frederiksen, H. Lin, E. D. Maloney, and C. Schumacher, 2017: Review of tropical-extratropical teleconnections on intraseasonal time scales. *Rev. Geophys.*, **55**, 902-937. doi: 10.1002/2016RG000538

Vangaugh, C., L. Buja, A. Kruczkiewicz, and L. Goddard, 2016: Identifying research priorities to advance climate services. *Climate Services*, **4**, 65-74. doi:10.1016/j.cliser.2016.11.004

Vitart, F. C. Ardilouze, A. Bonet, A. Brookshaw, M. Chen, C. Codorean, M. Deque, L. Ferranti, M. Fuentes, H. Hendon, J. Hodgson, H. -S. Kang, A. Kumar, H. Lin, G. Liu, X. Liu, P. Malguzzi, I. Mallas, M. Manoussakis, D. Mastrangelo, C. MacLachlan, P. McLean, A. Minami, R. Mladek, T. Nakazawa, S. Najam, Y. Nie, M. Rixen, A. W. Robertson, P. Ruti, C. Sun, Y. Takaya, M. Tolstykh, F. Venuti, D. Waliser, S. Woolnough, T. Wu, D. -J., Won, H. Xiao, R. Zaripov, and L. Zhang, 2017: The subseasonal to seasonal (S2S)

prediction project database. *Bull. Amer. Meteorol. Soc.*, **98**, 163-173. doi: 10.1175/BAMS-D-16-0017.1.

Vitart, F., 2017: Madden-Julian oscillation prediction and teleconnections in the S2S database. *Quart. J. Roy. Meteor. Soc.*, **143**, 2210-2220. doi:10.1002/qj.3079.

Vitart, F., Ardilouze, C., Bonet, A., Brookshaw, A., Chen, M., Codorean, C., Déqué, M., Ferranti, L., Fucile, E., Fuentes, M., Hendon, H., Hodgson, J., Kang, H.-S., Kumar, A., Lin, H., Liu, G., Liu, X., Malguzzi, P., Mallas, I., Manoussakis, M., Mastrangelo, D., MacLachlan, C., McLean, P., Minami, A., Mladek, R., Nakazawa, T., Najm, S., Nie, Y., Rixen, M., Robertson, A. W., Ruti, P., Sun, C., Takaya, Y., Tolstykh, M., Venuti, F., Waliser, D., Woolnough, S., Wu, T., Won, D.-J., Xiao, H., Zaripov, R., & Zhang, L. (2017). The Subseasonal to Seasonal (S2S) Prediction Project Database, *Bull. Amer. Meteorol. Soc.*, **98**, 163-173. doi: 10.1175/BAMS-D-16-0017.1

Vogel, J., M. J. Kolian, A. St. Juliana, H. Hosterman, J. Peers, D. Krishland, and K. Carney, 2020: Past is prologue: A case study exploration of the role of climate indicators in adaptation in the United States. *Climate Services*, **20**, doi:10.1016/j.cliser.2020.100202.

Wallace, J. M., G. Lim, and M. L. Blackmon, 1988: Relationship between cyclone tracks, anticyclone tracks and baroclinic waveguides. *J. Atmos. Sci.*, **45**, 439–462, https://doi.org/10.1175/1520-0469(1988)045,0439:RBCTAT.2.0.CO;2.

Wang, J., H. M. Kim, D. Kim, S. A. Henderson, C. Stan, and E. D. Maloney, 2020: MJO teleconnections over the PNA region in climate models. Part I: Performance- and process-based skill metrics. *J. Climate*, **33**, 1051-1067. doi:10.1175/JCLI-D-19-0253.1.

Wheeler, M. C. and H. H. Hendon, 2004: An all-season real-time multivariate MJO index: Development of an index for monitoring and prediction. *Mon. Wea. Rev.*, **132**, 1917-1932. doi:10.1175.1520-0493(2004)132<1917:AARMMI>2.0CO;2.

White, C.J., H. Carlsen, A. W. Robertson, R. J. Klein, K. K. Lazo, A. Kumar, F. Vitart, E. Coughlan de Perez, A. J. Ray, V. Murray, S. Bharwani, D. MacLeod, R. James, L. Fleming, A. P. Morse, B. Eggen, R. Graham, E. Kjellström, E. Becker, K. V. Pegion, N. J. Holbrook, D. McEvoy, M. Depledge, S. Perkins-Kirkpatrick, T. J. Brown, R. Street, L. Jones, T.A. Remenyi, I. Hodgson-Johnston, C. Buontempo, R. Lamb, H. Meinke, B. Arheimer, and S. E. Zebiak, 2017: Potential applications of subseasonal-to-seasonal (S2S) predictions. *Met. Apps.*, **24**, 315-325. doi:10.1002/met.1654.

Wilks, D. S., 2006: *Statistical methods in the atmospheric sciences*. 2nd ed. Academic press, 627 pp.

Yau, A. M.W., and E. K. M.Chang, 2020: Finding storm track activity metrics that are highly correlated with weather impacts. Part I: Frameworks for evaluation and accumulated track activity, *J. Climate*, **33**, 10169-10186. doi:10.1175/JCLI-D-20-0393.1.

Zhang, C., 2013: Madden-Julian Oscillation: Bridging weather and climate. *Bull. Amer. Meteorol. Soc.*, **94**, 1849–1870. doi:10.1175/BAMS-D-12-00026.1.

Zheng, C., E. K. -M. Chang, H. -M. Kim, M. Zhang, and W. Wang, 2018: Impacts of the Madden-Julian oscillation on storm-track activity, surface air temperature, and precipitation over North America. *J. Climate.*, **31**, 6113-6134. doi:10.1175/JCLI-D-17-0534.1.

Table 1: Description of native model resolution and reforecast (Rfc.) characteristics used in the analysis of this study. The frequency denotes how many times the reforecast is initialized during a week or month. The ensemble size describes how many ensemble members correspond to each initial condition. Model version indicates the version of the model used to generate the reforecast data used in this study.

Model	Horizontal/Vertical levels	Rfc. period	Rfc. frequency	Rfc. ens. size	Model Version
BoM	2.5^0x2.5^0/L17	1981-2013	6/month: 1st, 6th, 11th, 16th, 21st, & 26st	33	2014-01-01
CMA	1^0x1^0/L40	1994-2014	daily*	4	2014-05-01
CNR-ISAC	0.8^0x0.56^0/L54	1981-2010	every 5 days	5	2017-06-08
CNRM	0.7^0x0.7^0/L91	1993-2014	4/month: 1st, 8th, 15th, & 22nd	15	2014-12-01
ECCC	0.45^0x0.45^0/L40	1998-2017	weekly: Thu	4	Nov-Dec: 2019 & Jan-Mar 2020; Aug-Sep 2019 & May-Jul: 2020
ECMWF	0.15^0x0.15^0 days 0-15 0.3^0x0.3^0 after day 15 /L91	1999-2019	2/week: Mon & Thu	11	Nov-Dec: 2019 & Jan-Mar: 2020; Jul-Sep: 2019 & May-Jun: 2020
HMCR	1.1^0x1.4^0/L40	1985-2010	weekly: Thu	10	Nov-Dec: 2019 & Jan-Mar 2020; Jun-Sep: 2019 & May 2020
JMA	0.5^0x0.5^0/L60	1981-2012	3/month: 10th, 20th, & last day of the month	5	2017-01-31
KMA	1.5^0x1.5^0/L85	1991-2010	4/month; 1st, 9th, 16th, & 25th	3	Nov-Dec: 2019 & Jan-Mar 2020; Jun-Sep 2019 & May 2020
NCEP	1.5^0x1.5^0/L64	1999-2010	daily*	4	2011-03-01
UKMO	0.5^0x0.8^0/L85	1993-2016	4/month; 1st, 9th, 16th, & 25th	7	Nov-Dec: 2019 & Jan-Mar 2020; May-Sep 2020

*For the analysis in this study the same frequency as for the BoM model has been used.
With the exception of the BoM model, all fields in the S2S database are interpolated to a common longitude×latitude horizontal grid with 1.5^0x1.5^0 resolution.

Fig. 1. a) June-November composite of anomalies of the magnitude of the 200-850 hPa vertical wind shear vector (m s^{-1}; see text for definition) 3 weeks after the MJO phases 7-8 for reanalysis and b)-l) for the S2S models (3 weeks forecast). Reforecasts are initialized when the observed MJO, based on the ERA-I RMM index, is in phases 7-8. Numbers on the right hand side above each panel represent the pattern correlations over the entire domain between ERA-I and reforecast. The rectangle with dashed line in a) represents the Main Develop Region (MDR). Stippling denotes areas where anomalies are different from zero at the 95% confidence level based on the bootstrap test.

Fig. 2. Same as Fig. 1, except for the MJO phases 4-5.

Fig. 3. (a) STRIPES index for geopotential height at 500 hPa from reanalysis for winter and (b) summer seasons between 1981-2017 for days 0-40. (c) and (d) Mean across the models of STRIPES index difference between reforecasts and reanalysis for weeks 2-3.

Fig. 4. The modeled fraction of the observed STRIPES index (calculated using sliding 2-week windows) for regions marked with a box in Fig. 3a for (a-c) boreal winter and Fig. 3b (d-e) boreal summer.

Fig. 5. Pattern CC and relative amplitude of S2S reforecast and reanalysis over the PNA region vs forecast lead days for MJO phases 2-3 (a, c), and 6-7 (b, d). Horizontal solid lines in a), c) represent the reference line of pattern CC at 0.5. Horizontal solid lines in b), d) represent the reference line above (below) which the Z500 anomalies are overestimated (underestimated) in S2S models. The grey shadings indicate the 95% confidence level determined by the bootstrap test. The lower boundary represents the minimum 2.5th percentile of the bootstrapping distribution among the models, and the upper boundary represents the maximum 97.5th percentile distribution among the models.

Fig. 6. Difference between MJO phases 5-6 and 1-2 for the S2S models (left) and reanalysis (right) as a function of forecast week for reforecasts initialized during boreal winter. (a, b) Area-weighted average (35-55°N, 190-220°E) of Z500 for the Northeast Pacific. (c, d) Midlatitude (40-80°N) zonal wave 1+2 meridional heat flux anomalies (v*T*) at 500 hPa and (e, f) 100 hPa. Reanalysis is subsampled to match the reforecast period of each model.

Fig. 7. Difference between MJO phases 5-6 and 1-2 for the S2S models (left) and reanalysis (right) as a function of forecast week for reforecasts initialized during the boreal winter. (a, b) U10 at 60^0N. (c, d) 70-90^0N area-weighted average of Z500 and Z100. Reanalysis is subsampled to match the reforecast period of each model. The HMCR model is missing from panels (a, b) because the S2S database does not contain U10 from this model.

Fig. 8. Normalized histograms of U10 (m/s) at 60^0N for NDJF forecasts for week 4 following the MJO phases 1-2 (blue), phases 5-6 (red), and all phases (black bars). The blue and red bars indicate the mean value of U10 during phases 1-2 and phases 5-6, respectively. The values in the top left of each panel indicate the difference in the mean of the distributions between phases 5-6 and 1-2. * indicates values that are significantly different from each other at the 95% confidence level using a bootstrap test. The HMCR model is not included in the analysis because the S2S database does not contain U10 from this model. Low top models include BoM, CMA, and CNR-ISAC.

Fig. 9. a) Composite of weeks 3-4 boreal winter extratropical cyclone activity of the ECMWF model when the reforecasts are initialized in the MJO phases 8-1 with amplitude larger than 1. Units in m^2/s^2. The black contours show the 95% significance from the result of the bootstrap test. b)-d) The same as a), but for phases 2-3, 4-5, and 6-7, respectively. e)-h) Similar to a)-d), but the composites are made by using reanalysis data during the ECMWF reforecast cases. i) The average of all composites of 11 models for phases 8-1. Each of the 11 composites is made in the same way as a) but using different models. j)-l) Similar to i) but

28

Accepted for publication in *Bulletin of the American Meteorological Society.* DOI 10.1175/BAMS-D-21-0130.1.

Brought to you by UNIVERSITY OF MD BALTIMORE COUNTY | Unauthenticated | Downloaded 03/18/22 02:18 PM UTC

for phases 2-3, 4-5, and 6-7, respectively. m) Similar to i), but for the average of all 11 reanalysis composites for phases 8-1. Each of the 11 composites is made in the same way as b) but using reforecast cases in different models. n)-p) Similar as m) but for phases 2-3, 4-5, and 6-7, respectively.

Fig. 10 a) The scatter plot of weeks 3-4 Z500 pattern correlation (x-axis) versus *eke*850 pattern correlation (y-axis) of each model over the Northern Hemisphere (20°N-80°N) when the reforecast is initialized in MJO phases 8-1 with amplitude larger than 1. Each dot represents one model. The pattern correlation of extratropical cyclone activity is calculated between model composite [e.g. Fig.9a)] and reanalysis composite averaged for all model cases [e.g. Fig.9m)]. The Z500 pattern correlation is calculated in a similar way as extratropical cyclone activity. The solid line shows the 1:1 line, and the correlation coefficient is displayed at the bottom right corner of the panel. b)-d) Similar as a), but for phases 2-3, 4-5, and 6-7 respectively. e)-h) Similar as a)-d), but for the North Pacific and North America sector (20°N-80°N; 120°E-90°W). i)-l) Similar as a)-d), but for the North Atlantic sector (20°N-80°N; 90°W-30°E).

Fig. 11. Composites of T2m anomaly in week 3 after the MJO phase 3 for a) reanalysis and b)-k) S2S models. Dotted areas denote anomalies statistically significant at the 0.05 level based on a bootstrap resampling calculation. Numbers in the upper right corners show the pattern correlation between reforecasts and reanalysis.

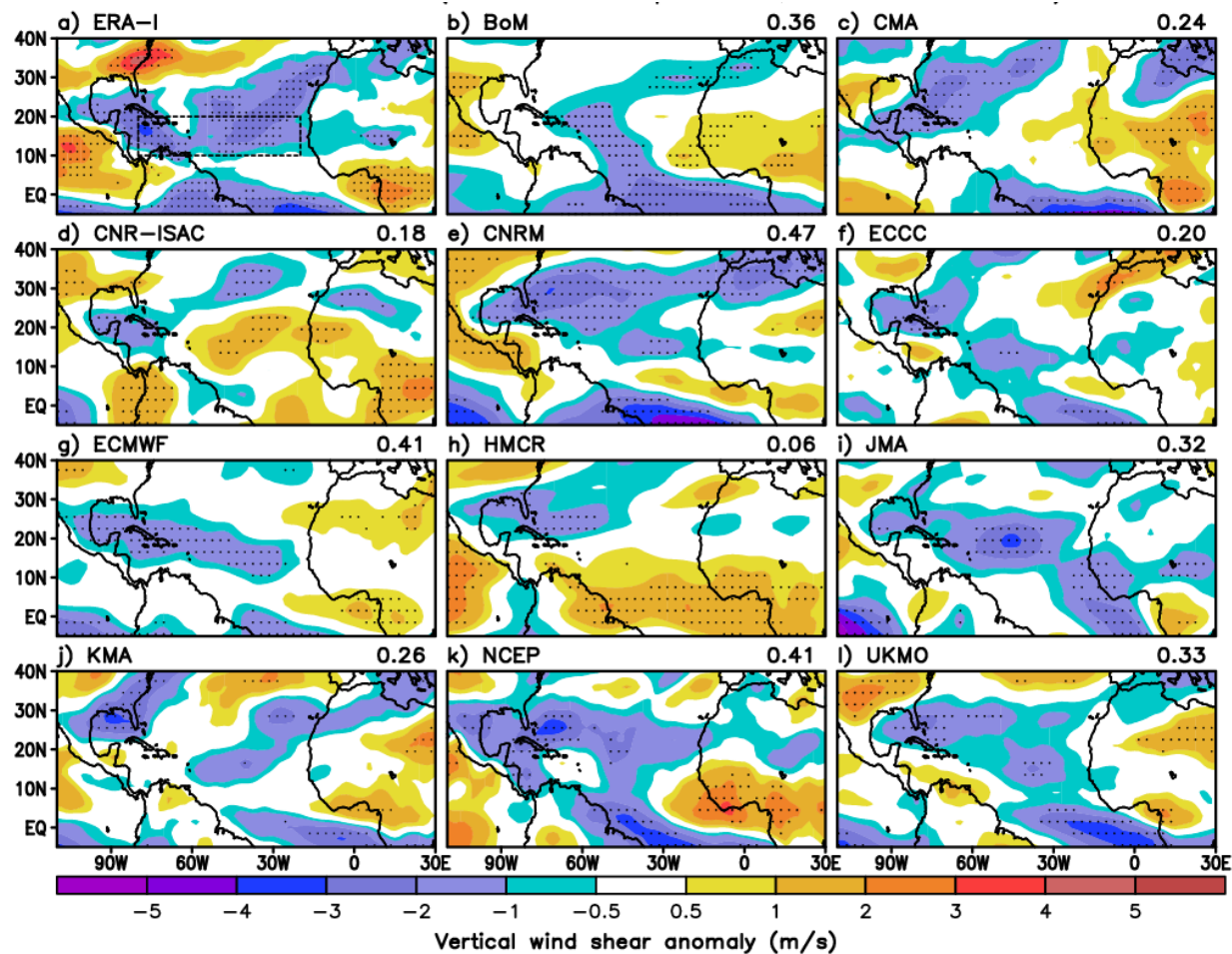Fig. 12. Same as Fig. 11, except for the MJO phase 7.

Fig. 1. a) June-November composite of anomalies of the magnitude of the 200-850 hPa vertical wind shear vector (m s^{-1}; see text for definition) 3 weeks after the MJO phases 7-8 for reanalysis and b)-l) for the S2S models (3 weeks forecast). Reforecasts are initialized when the observed MJO, based on the ERA-I RMM index, is in phases 7-8. Numbers on the right hand side above each panel represent the pattern correlations over the entire domain between ERA-I and reforecast. The rectangle with dashed line in a) represents the Main Develop Region (MDR). Stippling denotes areas where anomalies are different from zero at the 95% confidence level based on the bootstrap test.

Fig. 2. Same as Fig. 1, except for the MJO phases 4-5.

Fig. 3. (a) STRIPES index for geopotential height at 500 hPa from reanalysis for winter and (b) summer

seasons between 1981-2017 for days 0-40. (c) and (d) Mean across the models of STRIPES index difference

between reforecasts and reanalysis for weeks 2-3.

Fig. 4. The modeled fraction of the observed STRIPES index (calculated using sliding 2-week windows) for regions marked with a box in Fig. 3a for (a-c) boreal winter and Fig. 3b (d-e) boreal summer.
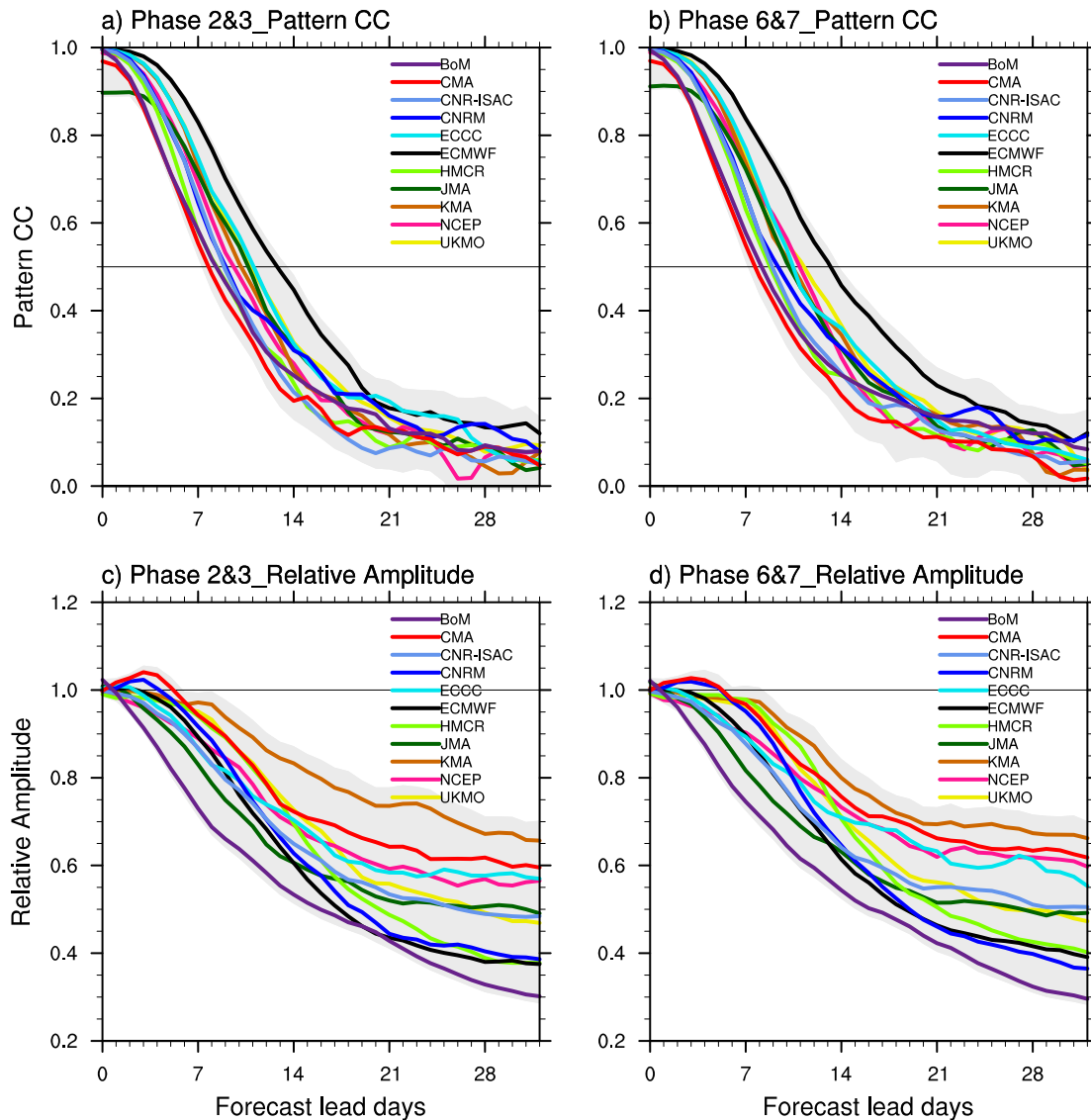
Fig. 5. Pattern CC and relative amplitude of S2S reforecast and reanalysis over the PNA region vs forecast lead days for MJO phases 2-3 (a, c), and 6-7 (b, d). Horizontal solid lines in a), c) represent the reference line of pattern CC at 0.5. Horizontal solid lines in b), d) represent the reference line above (below) which the Z500 anomalies are overestimated (underestimated) in S2S models. The grey shadings indicate the 95% confidence level determined by the bootstrap test. The lower boundary represents the minimum 2.5th percentile of the bootstrapping distribution among the models, and the upper boundary represents the maximum 97.5th percentile distribution among the models.
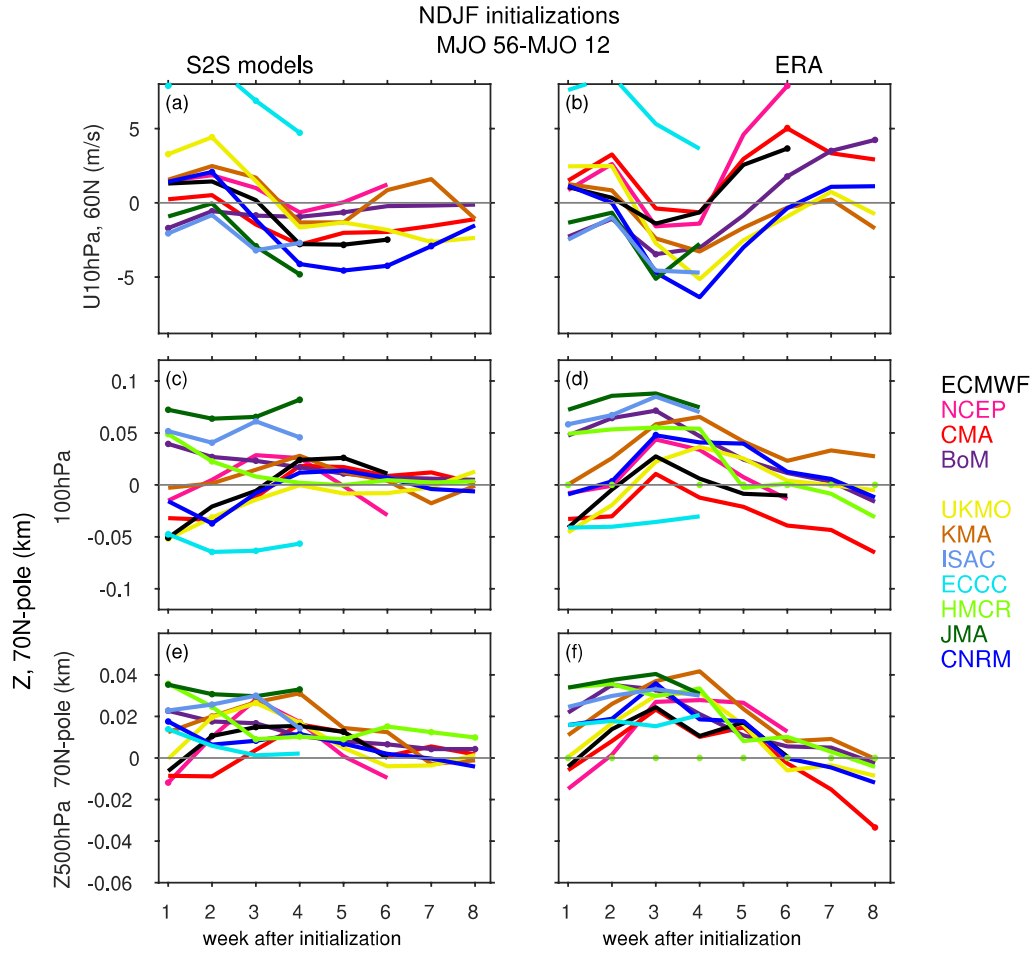
Fig. 6. Difference between MJO phases 5-6 and 1-2 for the S2S models (left) and reanalysis (right) as a function of forecast week for reforecasts initialized during boreal winter. (a, b) Area-weighted average (35-55°N, 190-220°E) of Z500 for the Northeast Pacific. (c, d) Midlatitude (40-80°N) zonal wave 1+2 meridional heat flux anomalies (v*T*) at 500 hPa and (e, f) 100 hPa. Reanalysis is subsampled to match the reforecast period of each model.

Fig. 7. Difference between MJO phases 5-6 and 1-2 for the S2S models (left) and reanalysis (right) as a function of forecast week for reforecasts initialized during the boreal winter. (a, b) U10 at 60^0N. (c, d) 70-90^0N area-weighted average of Z500 and Z100. Reanalysis is subsampled to match the reforecast period of each model. The HMCR model is missing from panels (a, b) because the S2S database does not contain U10 from this model.
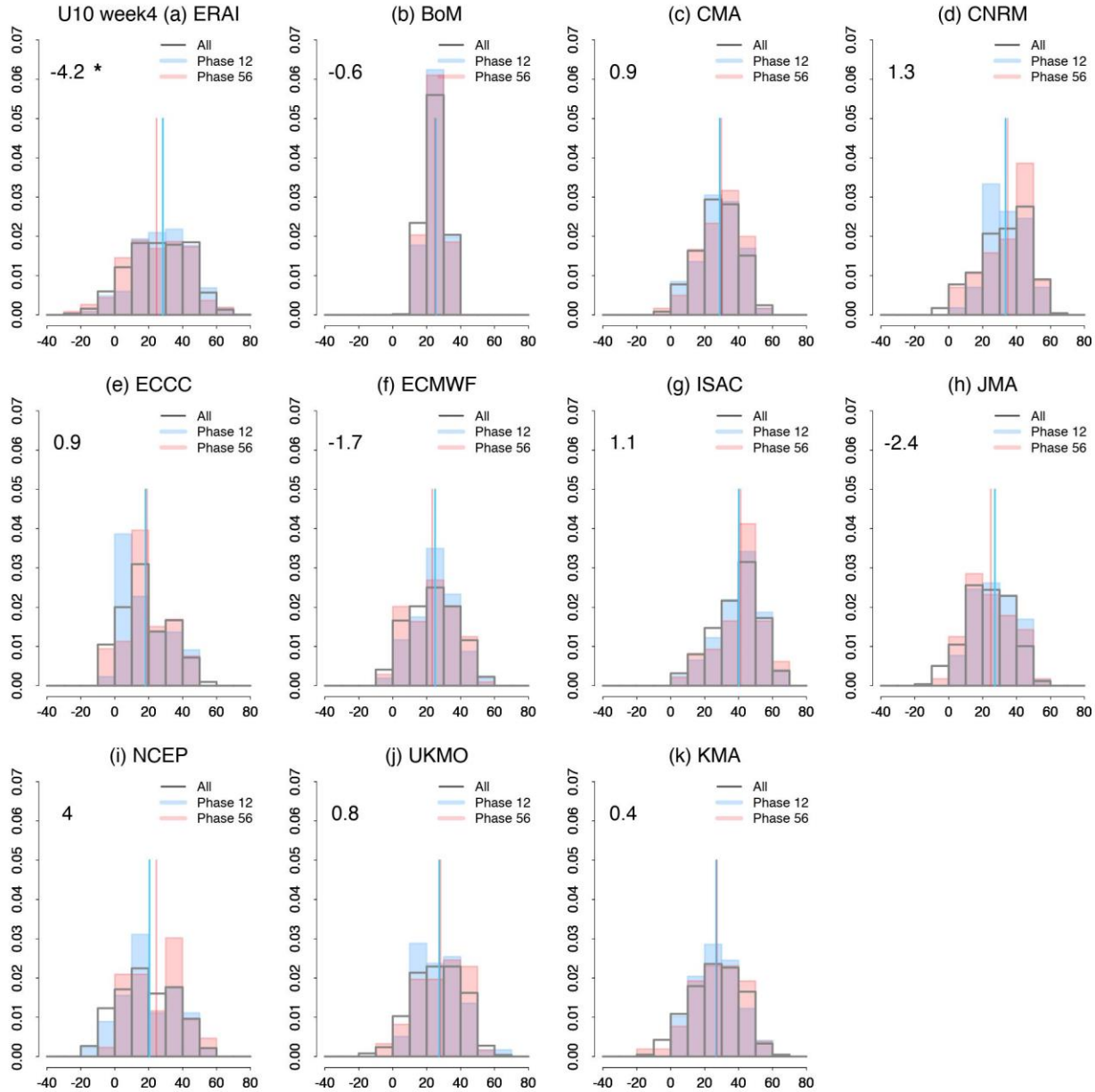
Fig. 8. Normalized histograms of U10 (m/s) at 60^0N for NDJF forecasts for week 4 following the MJO phases 1-2 (blue), phases 5-6 (red), and all phases (black bars). The blue and red bars indicate the mean value of U10 during phases 1-2 and phases 5-6, respectively. The values in the top left of each panel indicate the difference in the mean of the distributions between phases 5-6 and 1-2. * indicates values that are significantly different from each other at the 95% confidence level using a bootstrap test. The HMCR model is not included in the analysis because the S2S database does not contain U10 from this model. Low top models include BoM, CMA, and CNR-ISAC.
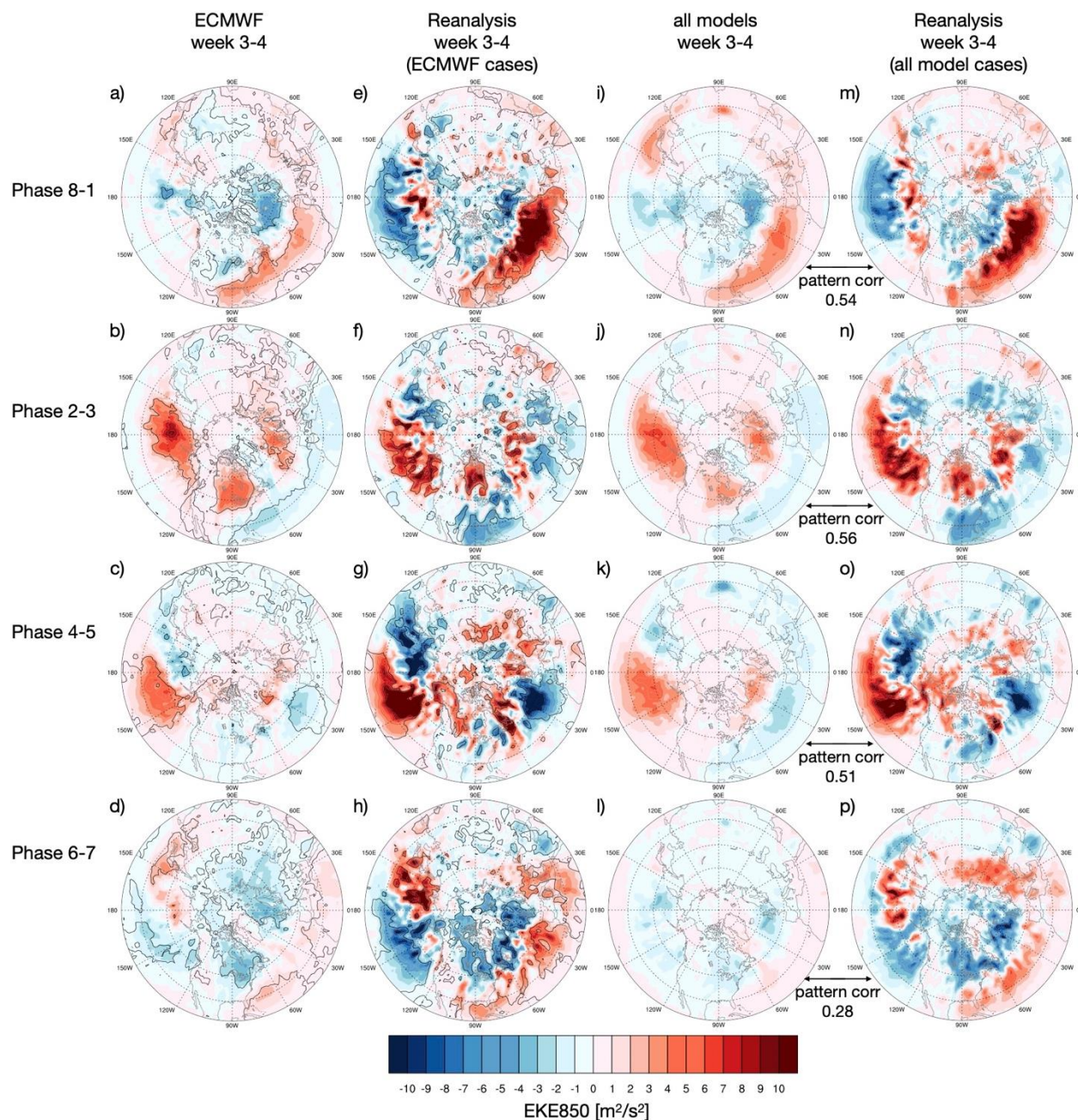
37

Fig. 9. a) Composite of weeks 3-4 boreal winter extratropical cyclone activity of the ECMWF model when the reforecasts are initialized in the MJO phases 8-1 with amplitude larger than 1. Units in m^2/s^2. The black contours show the 95% significance from the result of the bootstrap test. b)-d) The same as a), but for phases 2-3, 4-5, and 6-7, respectively. e)-h) Similar to a)-d), but the composites are made by using reanalysis data during the ECMWF reforecast cases. i) The average of all composites of 11 models for phases 8-1. Each of the 11 composites is made in the same way as a) but using different models. j)-l) Similar to i) but

for phases 2-3, 4-5, and 6-7, respectively. m) Similar to i), but for the average of all 11 reanalysis composites for phases 8-1. Each of the 11 composites is made in the same way as b) but using reforecast cases in different models. n)-p) Similar as m) but for phases 2-3, 4-5, and 6-7, respectively.
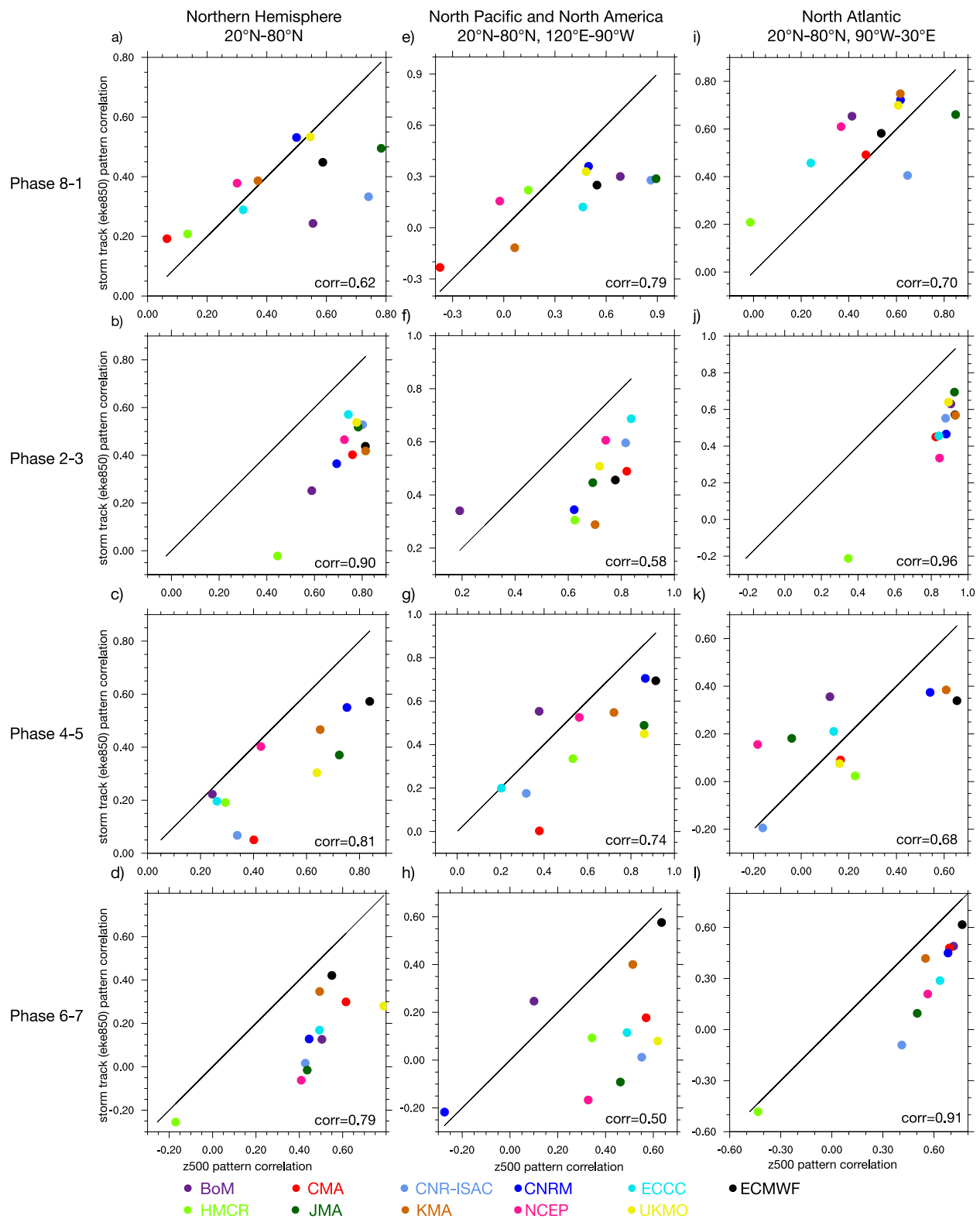
Fig. 10 a) The scatter plot of weeks 3-4 Z500 pattern correlation (x-axis) versus *eke*850 pattern correlation (y-axis) of each model over the Northern Hemisphere (20°N-80°N) when the reforecast is initialized in

MJO phases 8-1 with amplitude larger than 1. Each dot represents one model. The pattern correlation of extratropical cyclone activity is calculated between model composite [e.g. Fig.9a)] and reanalysis composite averaged for all model cases [e.g. Fig.9m)]. The Z500 pattern correlation is calculated in a similar way as extratropical cyclone activity. The solid line shows the 1:1 line, and the correlation coefficient is displayed at the bottom right corner of the panel. b)-d) Similar as a), but for phases 2-3, 4-5, and 6-7 respectively. e)-h) Similar as a)-d), but for the North Pacific and North America sector (20°N-80°N; 120°E-90°W). i)-l) Similar as a)-d), but for the North Atlantic sector (20°N-80°N; 90°W-30°E).
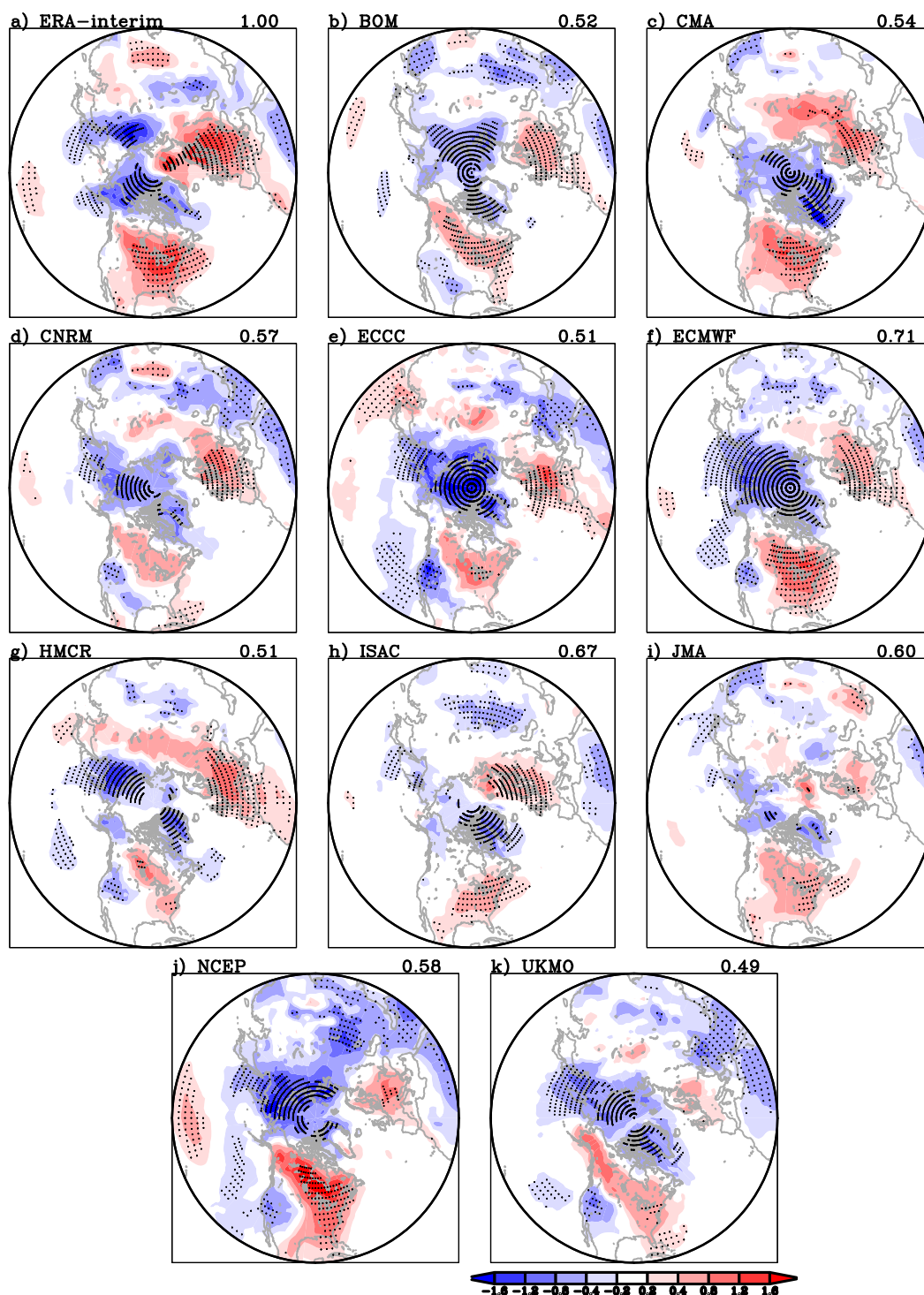
41

Fig. 11. Composites of T2m anomaly in week 3 after the MJO phase 3 for a) reanalysis and b)-k) S2S

models. Dotted areas denote anomalies statistically significant at the 0.05 level based on a bootstrap

resampling calculation. Numbers in the upper right corners show the pattern correlation between
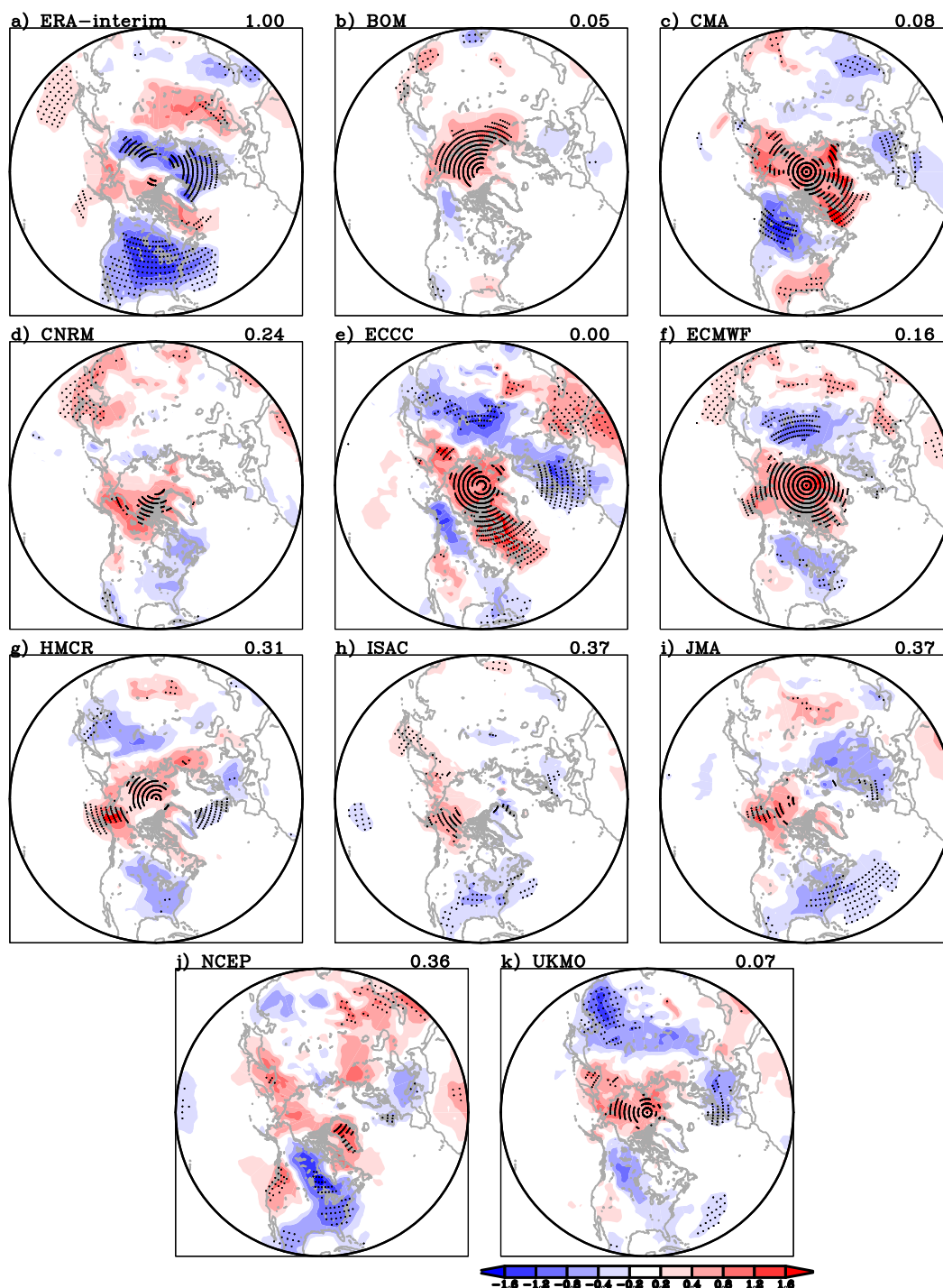
reforecasts and reanalysis.

Fig. 12. Same as Fig. 11, except for the MJO phase 7.